nature climate change

ARTICLES

https://doi.org/10.1038/s41558-020-0825-x

Increased melting level height impacts surface precipitation phase and intensity

Andreas F. Prein ✉ and Andrew J. Heymsfield

The global near-surface temperature increased by ~0.155 K per decade during 1979–2012, which resulted in decreasing snow and increasing rain events, retreating mountain glaciers and more frequent and intense rainfall extremes. Although surface temperature increases are well studied, less attention is given to the associated changes in the tropospheric thermal structure, such as melting level height, which affects cloud microphysics and surface precipitation. Here we use observations and reanalyses to show that the melting level height increased by 32 ± 14 m per decade over global land areas during 1979–2010, consistent with a warming atmosphere. This causes a transition from snow to rain, the enhanced melting of hail and an increased depth of warm cloud layers (cloud base to melting level distance). Warm cloud layers with a depth beyond ~3.5 km result in an intensification of extreme precipitation at twice the rate of the atmospheric moisture increases. Days with such environments increased by 25% per decade in populated regions, such as the eastern United States.

Global near-surface temperatures have increased by ~1 K since 1850 with a higher warming over land than over oceans[1]. The bulk of the warming occurred since the late 1970s. Although near-surface warming is well studied, less attention has been paid to warming at higher levels of the troposphere (the lowest layer of the Earth's atmosphere) other than studies that investigated changes in the vertical temperature profile[2–5]. Tropospheric temperatures directly impact the formation, composition and dynamics of clouds and therefore precipitation at the surface[6]. Particularly important for cloud processes and surface precipitation is the height of the melting level (ML), defined as the zero-degree wet-bulb temperature[7], above the surface. We use the wet-bulb temperature because an ice particle will not begin melting until the ambient wet-bulb temperature (or ice-bulb temperature) reaches 0 °C. The phase and size of hydrometeors determine their fall speed[8], which is, in turn, proportional to the precipitation rate at the surface. The fall speed of liquid drops ranges from 0.0003 m s^{-1} for small drops (diameter ~0.001 mm) to 9 m s^{-1} for very large drops (~6 mm; drops >3 mm have a high probability of breaking up into smaller drops)[9]. Snow falls at ~1 m s^{-1}, with rimed snow and graupel falling faster[10]. Large hail can reach velocities of more than 40 m s^{-1} (ref. [11]). The highest rainfall intensities are observed for clouds with large drops that fall fast and evaporate little before they reach the surface.

So far, there is poor quantitative understanding of how climate change affects ML heights and the corresponding surface precipitation characteristics. Here we document changes in ML heights and investigate their impacts on the precipitation phase and intensity by focusing on societally relevant processes, such as snowfall, damaging hail and heavy rain. For this purpose, we combined radiosonde sounding (RS) measurements and data from two reanalysis products to derive the best estimate of the effect of historic climate change on the ML height and related variables that span a common period from 1979 to 2010. The mid-troposphere is a poorly observed region and RSs[12] as well as reanalyses[13,14] are known to have homogeneity issues, which can result in spurious trend estimates. Therefore, we quality controlled all the records and removed those with spurious breaking points from the analyses (see Methods and Supplementary Fig. 1). All the results are presented with error margins based on the differences among the three datasets. The annual and seasonal absolute variabilites of quality-controlled ML heights at RS locations are remarkably similar between the three datasets; however, the European Centre for Medium-Range Weather Forecasts (ECMWF) Interim Reanalysis (ERA-Interim)[15] had systematically lower ML heights than the RS observations and ECMWF's Twentieth-Century Reanalysis (ERA-20C)[16] (Supplementary Fig. 2; note that the RS data are assimilated into ERA-Interim but not into ERA-20C). We used linear regression and piecewise linear fit models[17] that allow for non-linear trend estimates in annual and seasonal time series between 1979 and 2010, which is the common period covered by all datasets. Additionally, we show results from ERA-20C that reach back to 1900 and ERA-Interim and RS results covering up to 2017. Linear and piecewise linear trend estimates agree within 10%, which indicates that changes are mostly linear within the evaluation period (see Supplementary Fig. 3 for an example). For the sake of simplicity, we decided to show only linear trend estimates.

Over global land regions, the ML height has significantly increased by 32 ± 14 m per decade (dec^{-1}) from 1979 to 2010 (Fig. 1b). The ML height increases correlate well with the near-surface temperature (T2M, or air temperature measured 2 m above the surface) changes on continental scales. Globally, the rate of ML height increases per degree of surface warming was 206 ± 90 m K^{-1}. Interannual variability (Supplementary Fig. 2) and trends are more similar between the datasets in the Northern (Fig. 1d,f,h) than in the Southern (Fig. 1e,g,i) Hemisphere, probably due to the lower observation density in the latter. ML increases were highest in the ERA-20C and lower in the ERA-Interim and RS observations. The reanalysis datasets agree that the largest ML height increases occurred in the tropics and the northern mid-latitudes, whereas the Southern Ocean and Polar regions experienced small changes because the ML height is predominantly at the surface (Fig. 1k). The trends in ML heights are spatially more uniform than the T2M changes (Fig. 1j,k). Although T2M and the ML height increases correlate well on the global and continental scales (Fig. 1a-i), on regional scales, the rates of increase in the ML height per degree of T2M warming differ widely (Fig. 1l). The largest increases can be found over the ocean, as 47% of ocean areas exceed trends of

National Center for Atmospheric Research (NCAR), Boulder, CO, USA. ✉e-mail: prein@ucar.edu

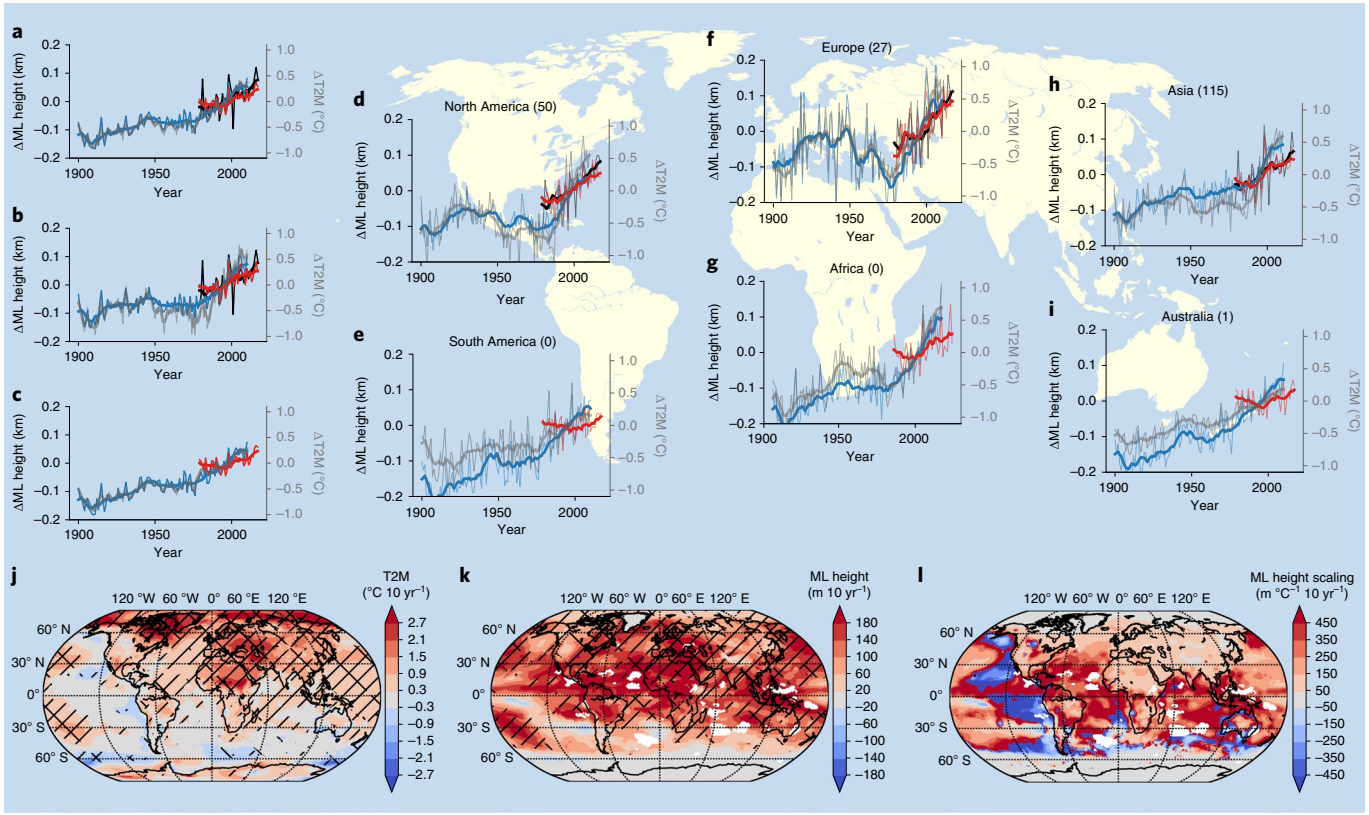

Fig. 1 | Annual average ML height changes (ΔML) since 1900. a–i, ΔML globally (**a**), over land (**b**), over ocean (**c**) and over continents (**d–i**). The thin blue and red lines show data from the ERA-20C and ERA-Interim, respectively, reanalyses and the thin black lines show the RS data. Surface temperature increases (ΔT2M) from ERA-20C are shown in grey (right-hand *y* axis). The thick lines show the ten-year running means of annually averaged data. The number of RS locations per continent is shown in the title of panels **d–i**. **j–l**, The average linear trend estimates from ERA-20C and ERA-Interim between 1979 and 2010 are shown for T2M (**j**), ML height (**k**) and ML height changes per degree local warming (**l**). Right and left tilted hatched areas indicate statistically significant trends in ERA-20C and ERA-Interim, respectively, based on a two-sided Wald test with *t*-distribution ($P = 0.05$).

300 m K^{-1} compared with only 13% of land regions. However, trends over ocean regions are more uncertain and dependent more on the reanalysis model due to the far lower density of observations compared with those of land regions. ML heights also increase in regions that experienced a cooling of T2M, which indicates a decoupling between local near-surface temperature trends and ML height trends, probably due to a decreasing lapse rate driven by convection in the convectively most-active regions. This decoupling probably occurs due to mixing and transport processes in the free troposphere that make the temperature field more homogeneous along the horizontal. Seasonally, large increases of over 65 m dec^{-1} occur in mid- and high-latitude regions over the Northern Hemisphere during June, July and August and September, October and November (Extended Data Fig. 1). The above results are based on all the days in the record, but ML height trends are similar for wet or dry days only (Supplementary Figs. 4–6).

A theoretical estimate of the ML height increases can be derived by assuming a constant standard atmosphere temperature lapse rate of –6.49 K km^{-1} (ref. [18]), which corresponds to an ML height increase of 154 m K^{-1}. This is lower than, but still within the error margins of, our estimate of 206 ± 90 m K^{-1}. Such differences can occur due to the simplicity of these assumptions, uncertainties in ML height records, changes in low-level relative humidity and changes in the tropospheric lapse rate. Low-level relative humidity did not change significantly in the RS records (Supplementary Fig. 6), but tropospheric lapse rates are expected to stabilize under global warming, which would result in smaller lapse rates that, in turn, accelerate ML height increases[3,4]. Our results are consistent with this expectation and show a predominant increase in surface-to-ML-height lapse rates (Extended Data Fig. 2). Our ML height increase estimate of 206 ± 90 m K^{-1} corresponds to an average temperature lapse rate of –4.9 (–8.6 to 3.4) K km^{-1} given a warming of 1 °C. These changes are, however, much more uncertain than changes in ML height (Supplementary Fig. 7) and vary in magnitude and sign between datasets and regions.

An expected consequence of increasing ML heights is a decrease in snowfall and an increase of rainfall events, here measured as a decreasing snow-day to precipitation-day ratio (Extended Data Fig. 3 and Supplementary Fig. 8). Results from ERA-20C suggest that this ratio was constant or increased between 1900 and 1980 in North America, Europe and Asia. All the datasets show significant decreases between 1979 and 2010, by –1.0 ± 0.2% dec^{-1} in Europe, –1.4 ± 0.6% dec^{-1} in Asia and –0.5 ± 0.4% dec^{-1} in North America, in agreement with previous work[19,20]. The lower decreases in North America and the large increase in Scandinavia and western Russia are partly related to climate internal variability[20].

Another potential consequence of increasing the ML heights is an increase in the depth of the warm cloud layer (WCL)—the distance between the cloud base height (lifting condensation level) and the ML height, if the cloud base height increases by less than the ML height. The WCL depth influences the liquid water content in the cloud and precipitation rates at the surface because large, fast-falling drops form very efficiently by collision and coalescence (warm rain process) in clouds with deep WCLs[6]. This is supported by

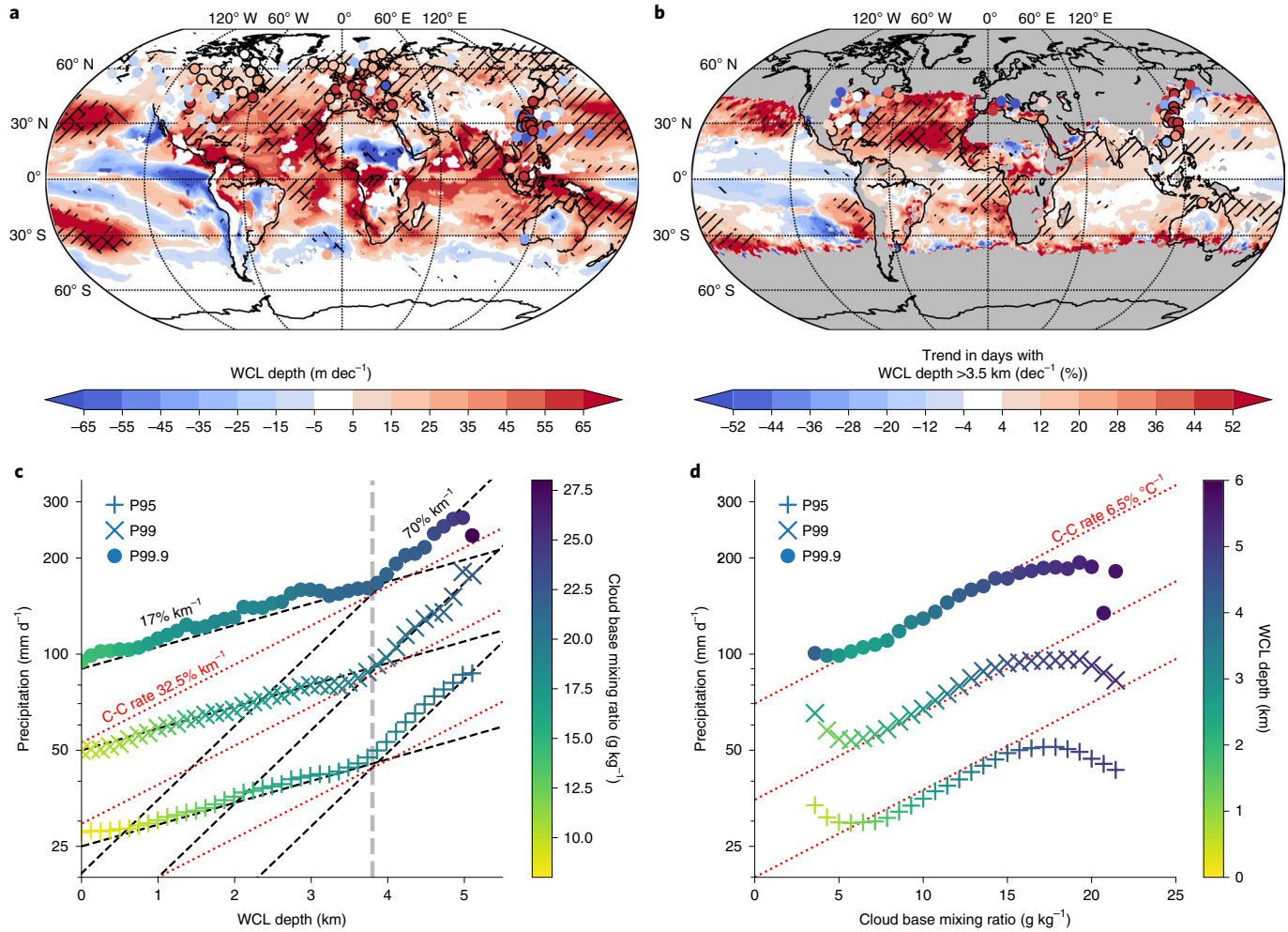

Fig. 2 | WCL depths increased over the period 1979–2010 on days with more than 1 mm of precipitation, which enhanced the risk for extreme rainfall. **a**, Linear trends in the annual average WCL depth on precipitation days showing average ERA-20C and ERA-Interim (contours) and RS (dots) trends. Right and left tilted hatches show significant trends in ERA-20C and ERA-Interim, respectively, and black circles show significant trends in RS data based on a two-sided Wald test with *t*-distribution ($P = 0.05$). **b**, Similar to **a**, but for frequency increases of days with WCL depths deeper than 3.5 km. **c**, Relationship between daily average RS WCL depth and daily precipitation accumulation from MSWEP V2 (Multi-Source Weighted-Ensemble Precipitation version 2) for the 95, 99 and 99.9 percentiles (P95, P99 and P99.9, respectively) within 100-m bins with an overlap of ±250 m. Black dashed lines show exponential function fits for increases of 17% km^{-1} (below a WCL depth of 3.5 km) and 70% km^{-1} (above a WCL depth of 3.5 km), and red dotted lines show the expected increases from the Clausius–Clapeyron (C-C) relationship. Colours show the average cloud base mixing ratio. **d**, Similar to **c**, but showing the cloud base mixing ratio versus extreme rainfall rates; the colours correspond to the average WCL depth.

observational studies, which show that precipitation intensity responds non-linearly with a deepening of clouds[21] and precipitation efficiency increases with mid-tropospheric humidity[22].

Over global land regions, thee WCL depth increased by 15 ± 12 m dec^{-1} from 1979 to 2010 on days with more than 1 mm d^{-1} rainfall (Fig. 2a). The uncertainty range of the changes in WCL depth (and changes in cloud base height) is large compared to that of changes in the ML height. RS and ERA-20C show significant increases in most land areas, whereas positive (in the northern mid-latitudes) and negative (in the tropics) trends cancel out in ERA-Interim (Extended Data Figs. 4 and 5). WCL depth increases of over 65 m dec^{-1} are found in June, July and August in many Northern Hemisphere mid-latitude regions (Extended Data Fig. 5). This agrees with high-resolution climate change simulations, which show a deepening of the WCL by ~200 m K^{-1} in the vicinity of heavy precipitation convective storms in the United States by the end of the century[4]. WCL change is mainly driven by increases in the ML height rather than by the cloud base height. The latter is less systematic and more uncertain (Extended Data Fig. 4),which agrees with observational results[23]. Using 10 mm d^{-1} instead of 1 mm d^{-1} as the precipitation threshold to identify wet days has minor impacts on the ML height trends, but decreases the cloud base height trends from 2 m to −23 m dec^{-1}. This results in an enhanced deepening of the WCL depth for more intense precipitation events (Supplementary Fig. 5). A consequence of the deepening WCL is a more active warm rain process within clouds. An exponential relationship between heavy rainfall at the surface and the WCL depth is observed at RS locations (Fig. 2c). The rate of increase is 17% km^{-1} for WCLs up to ~3.5 km. This corresponds to approximately half the rate that is expected from atmospheric moisture increases (Clausius–Clapeyron relationship), which is 32.5% km^{-1}, assuming a moist adiabatic lapse rate of 5 K km^{-1} and a saturation vapour pressure increase of 6.5% per degree of warming (that is, 5 K km^{-1} × 6.5% K^{-1} = 32.5% km^{-1}). The rate of extreme rainfall increases fourfold (70% km^{-1}) in environments with WCLs deeper than ~3.5 km, which corresponds to double the Clausius–Clapeyron rate. A similar transition can be

seen for mean precipitation (not shown). Using the WCL depth derived from ERA-Interim for the scaling analysis results in even stronger responses of extreme precipitation to a deepening of WCLs beyond ~3 km, especially over ocean regions (Supplementary Fig. 9). These results are in agreement with weather forecasting guidance, which relates environments with a WCL depth >3.3 km to flash flood events[24,25]. This steep increase is probably due to the increasing rainfall efficiency related to the collision and coalescence of raindrops (warm rain process) in clouds with deep WCLs[22] and higher water vapour contents available for condensation (Fig. 2c)[26], and might also be associated with an enhanced organization of convective storms (Extended Data Fig. 6). Extreme precipitation intensifies with the convective available potential energy (CAPE) up to 1,000 J kg^{-1}. Further increases in CAPE do not result in the further intensification of extreme precipitation[27] (Extended Data Fig. 6).

Environments with a WCL depth >3.3 km mainly occur in the tropics and extend into mid-latitudes during the warm season (Extended Data Fig. 6). Extreme precipitation events in these areas are mainly related to mesoscale convective systems and tropical cyclones. Many land regions experienced significant increases in days with WCL depths >3.5 km, with values of 25% dec^{-1} in the eastern United States from 1979 to 2010 (Fig. 2b). Extreme precipitation increased with cloud base mixing ratios at the Clausius–Clapeyron rates at a maximum (Fig. 2d), which is in line with theory and previous studies that related extreme precipitation changes with near-surface temperature and humidity[28–31]. We see similar transitions in scaling rates when we constrain our RS-based analyses to tropical regions, North America and Europe (Supplementary Fig. 10).

Increasing the ML heights and WCL depths also causes an enhanced melting of hailstones because they fall through a deeper and warmer layer before they reach the surface. Hail observations from the United States and Australia show that damaging hail with maximum diameters larger than 50 mm rarely occurs in environments with ML heights above 4.5 or 3.8 km (ERA-20C or ERA-Interim, respectively) (Fig. 3a), because of the enhanced melting of hail[32,33] (the lower threshold in ERA-Interim is due to a systematically lower ML height in this dataset; Supplementary Fig. 2). Such high MLs are typically found in the tropics and subtropics, but can extend into the mid-latitudes during the warm season. The increasing ML height results in a non-significant reduction of potential damaging-hail frequencies (Fig. 3b). This is due to an increasing trend in the ratio of days with severe convection environments (significant severe parameter (SSP) > 10,000 m^3 s^{-3} (ref. [34])) that also have MLs higher than 3.8 or 4.5 km (ERA-Interim or ERA-20C, respectively) (Fig. 3b). The largest trends in potential hail-frequency reductions are found in the tropics. However, the SSP tends to overestimate damaging-hail risks in this region[35], which raises the question whether this reduction translates into a real decrease in damaging-hail hazards. Trends also start to emerge in some of the world's hail hot spots in the central United States, Argentina, southeast China and the foothills of the Himalayas. However, most of these trends are not significant regionally due to the large interannual variability in severe convective environments. Over global land regions, the ratio of days with severe convective environments and MLs higher than 3.8 or 4.5 km (ERA-Interim or ERA-20C, respectively) relative to all severe convective days increases significantly by 1.3 ± 0.2% dec^{-1} (Fig. 3c). These results agree with hail modelling studies that show a significant decrease in damaging hail frequencies in subtropical regions due to an enhanced melting under future

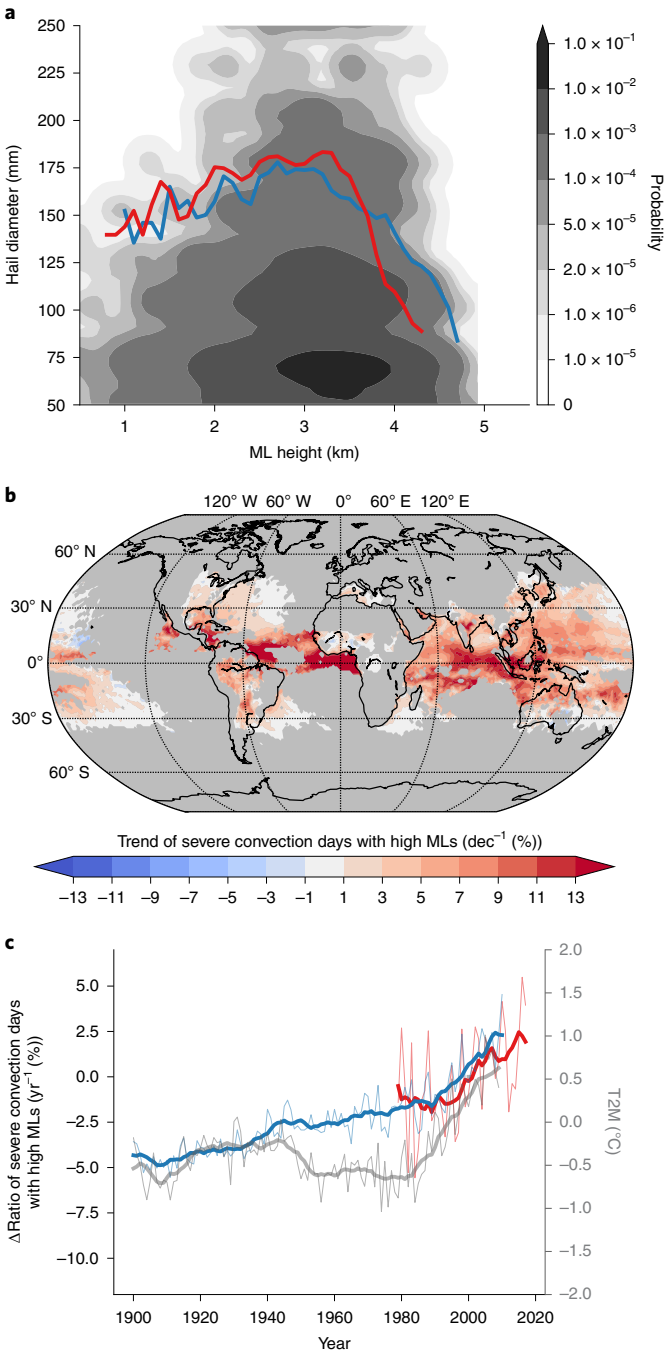

Fig. 3 | Increases in ML height (above the surface) reduce the risk of damaging hail in tropical and subtropical regions due to enhanced melting. a, The kernel density plot shows the probability distribution of daily mean ERA-20C ML heights and observed maximum hail diameters at the surface. The red and blue lines show the 99th percentile of hail diameters for 400-m-wide bins calculated every 100 m (an overlap of 300 m between bins) for ERA-Interim and ERA-20C, respectively. **b**, Mean linear trend estimates from ERA-Interim and ERA-20C (filled coloured contours) of the annual ratio between days that have favourable severe convective environments but with MLs that are too high and all favourable days. The latter feature SSPs[34] that are larger than 10,000 m^3 s^{-3} and the former additionally have ML heights >4.5 or 3.8 km in ERA-20C or ERA-Interim, respectively. Most of the changes are non-significant. **c**, Annual average changes in this ratio over global land in the ERA-20C and ERA-Interim reanalyses (thin blue and red lines, respectively). The corresponding surface temperature increases (ΔT2M) from ERA-20C are shown as a thin grey line (right-hand *y* axis). Thick lines show the ten-year running means of annually-averaged data (thin lines).

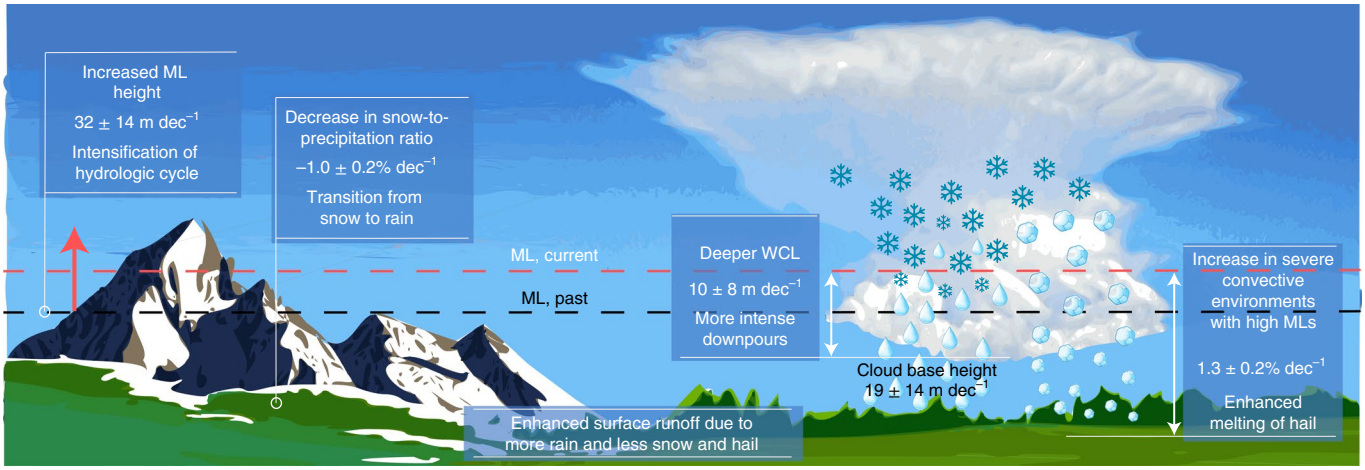

Fig. 4 | Increasing ML heights results in decreases in the surface snowfall, increases in heavy rainfall, an enhanced melting of hail and an accelerated surface runoff. Over land, ML heights increase by 32 ± 14 m dec^{-1}, which results in significant decreases in the snowfall-to-rainfall ratio in northern latitudes. This increase also results in an enhanced melting of hail, which reduces the risk of damaging hail by 1.3 ± 0.2% dec^{-1}, particularly in tropical and subtropical regions. The WCL depth of precipitating clouds increases at rates of 10 ± 8 m dec^{-1}, which results in an increased risk for rainfall events that produce flash floods. Shown are the mean trends and spread based on results from RS, ERA-Interim and ERA-20C data.

climate change[33]. The enhanced melting could, however, increase future flood risk, as heavy precipitation that arrives at the surface as rain instead of hail substantially increases runoff[32,36].

Our main results are summarized in Fig. 4. We show that the ML heights increased from 1979 to 2010 in most land areas at an average rate of 32 ± 14 m dec^{-1}. The rates of ML height increases per degree of near-surface warming frequently exceed 300 m K^{-1} in the tropics and subtropics. The reasons for these large changes are unclear and demand future investigations, but significant increases in the atmospheric lapse rates over ocean regions are identified as one contributor. A continuation of the ML height trends into the future could have substantial impacts on tropical glaciers and associated water resources[37,38].

The ML height increases result in a significant reduction of snow events and a corresponding increase in rain events in the Northern Hemisphere regions and seasons with close to freezing-level temperatures, in agreement with previous studies[19].

The global land average WCL depth on precipitation days increased by 10 ± 8 m K^{-1} with the increases frequently exceeding 65 m K^{-1} in northern mid-latitudes during the warm season. The deepening of the WCL depth resulted in a rapid increase in the frequency of environments associated with downpours (WCLs deeper than 3.5 km) on the order of 10–20% dec^{-1} from 1979 to 2010. The deepening of WCLs beyond 3.5 km and the associated changes in cloud microphysics and dynamics could be partly responsible for the observed extreme precipitation increases[39] that are larger than the saturation moisture increases (the latter increase according to the Clausius–Clapeyron relationship at 6.5% per degree of warming[40]). Our results suggest that climate change could result in an intensification of precipitation extremes beyond the Clausius–Clapeyron rates. The possibility of this so-called super Clausius–Clapeyron scaling is actively debated in the scientific literature[30,41–43].

ML height increases also result in the additional melting of small hail in all the regions and a reduction of large-hail frequency (25 mm diameter or larger) in tropical and subtropical regions, consistent with hail modelling studies[32,33]. However, melting-related decreases are contrasted by a general lack of frequency trends in observed damaging hail[44,45].

In general, increases in the ML height accelerate the hydrological cycle in all seasons due to a transition from solid to liquid precipitation and an increasing rate of environments that produce extreme rainfall. Additionally, increases in ML height might also affect cloud properties such as cloud brightness and spatiotemporal structures. Assessing the ability of climate models to reproduce historical changes in ML heights and associated effects on surface precipitation should be the focus of future investigations.

Online content

Any methods, additional references, Nature Research reporting summaries, source data, extended data, supplementary information, acknowledgements, peer review information; details of author contributions and competing interests; and statements of data and code availability are available at https://doi.org/10.1038/s41558-020-0825-x.

Received: 5 December 2019; Accepted: 18 May 2020;
Published online: 29 June 2020

References

1. IPCC *Climate Change 2013: The Physical Science Basis* (eds Stocker, T. F. et al.) (Cambridge Univ. Press, 2013).
2. O'Gorman, P. A. & Singh, M. S. Vertical structure of warming consistent with an upward shift in the middle and upper troposphere. *Geophys. Res. Lett.* **40**, 1838–1842 (2013).
3. Kröner, N. et al. Separating climate change signals into thermodynamic, lapse-rate and circulation effects: theory and application to the European summer climate. *Clim. Dyn.* **48**, 3425–3440 (2017).
4. Prein, A. F. et al. Increased rainfall volume from future convective storms in the US. *Nat. Clim. Change* **7**, 880–884 (2017).
5. Pithan, F. & Mauritsen, T. Arctic amplification dominated by temperature feedbacks in contemporary climate models. *Nat. Geosci.* **7**, 181–184 (2014).
6. Pruppacher, H. R., & Klett, J. D. *Microphysics of Clouds and Precipitation* (Springer Science, Business Media, 2012).
7. Wilson, W. T. An outline of the thermodynamics of snow-melt. *Eos Trans. Am. Geophys. Union* **22**, 182–195 (1941).
8. Beard, K. V. Terminal velocity and shape of cloud and precipitation drops aloft. *J. Atmos. Sci.* **33**, 851–864 (1976).
9. Foote, G. B. & Du Toit, P. Terminal velocity of raindrops aloft. *J. Appl. Meteorol.* **8**, 249–253 (1969).
10. Böhm, H. P. A general equation for the terminal fall speed of solid hydrometeors. *J. Atmos. Sci.* **46**, 2419–2427 (1989).
11. Heymsfield, A. J., Giammanco, I. M. & Wright, R. Terminal velocities and kinetic energies of natural hailstones. *Geophys. Res. Lett.* **41**, 8666–8672 (2014).
12. Gaffen, D. J. Temporal inhomogeneities in radiosonde temperature records. *J. Geophys. Res. Atmos.* **99**, 3667–3676 (1994).
13. Thorne, P. & Vose, R. Reanalyses suitable for characterizing long-term trends. *Bull. Am. Meteorol. Soc.* **91**, 353–362 (2010).
14. Bosilovich, M. G., Robertson, F. R. & Chen, J. Global energy and water budgets in MERRA. *J. Clim.* **24**, 5721–5739 (2011).

15. Dee, D. P. et al. The ERA-Interim reanalysis: configuration and performance of the data assimilation system. *Q. J. R. Meteorol. Soc.* **137**, 553–597 (2011).
16. Poli, P. et al. ERA-20C: an atmospheric reanalysis of the twentieth century. *J. Clim.* **29**, 4083–4097 (2016).
17. Tomé, A. & Miranda, P. Piecewise linear fitting and trend changing points of climate parameters. *Geophys. Res. Lett.* **31**, L02207 (2004).
18. Sissenwine, N., Dubin, M. & Wexler, H. The US standard atmosphere, 1962. *J. Geophys. Res.* **67**, 3627–3630 (1962).
19. Tamang, S. K., Ebtehaj, A. M., Prein, A. F. & Heymsfield, A. J. Linking global changes of snowfall and wet-bulb temperature. *J. Clim.* **33**, 39–59 (2020).
20. Guo, R., Deser, C., Terray, L. & Lehner, F. Human influence on winter precipitation trends (1921–2015) over North America and Eurasia revealed by dynamical adjustment. *Geophys. Res. Lett.* **46**, 3426–3434 (2019).
21. Wood, R. Stratocumulus clouds. *Monthly Weather Rev.* **140**, 2373–2423 (2012).
22. Narsey, S. et al. Convective precipitation efficiency observed in the tropics. *Geophys. Res. Lett.* **46**, 13574–13583 (2019).
23. Sun, B., Karl, T. R. & Seidel, D. J. Changes in cloud-ceiling heights and frequencies over the United States since the early 1950s. *J. Clim.* **20**, 3956–3970 (2007).
24. Doswell, C. A. in *Severe Convective Storms* (Ed. Doswell, C. A.) 1–26 (Springer, 2001).
25. Davis, R. S. in *Severe Convective Storms* (Ed. Doswell, C. A.) 481–525 (Springer, 2001).
26. Beard, K. V. & Ochs, H. T. III Warm-rain initiation: an overview of microphysical mechanisms. *J. Appl. Meteorol.* **32**, 608–625 (1993).
27. Barbero, R. et al. A synthesis of hourly and daily precipitation extremes in different climatic regions. *Weather Clim. Extremes* **26**, 100219 (2019).
28. O'Gorman, P. A. Precipitation extremes under climate change. *Curr. Clim. Change Rep.* **1**, 49–59 (2015).
29. Ban, N., Schmidli, J. & Schär, C. Evaluation of the convection-resolving regional climate modeling approach in decade-long simulations. *J. Geophys. Res. Atmos.* **119**, 7889–7907 (2014).
30. Prein, A. F. et al. The future intensification of hourly precipitation extremes. *Nat. Clim. Change* **7**, 48–52 (2017).
31. Zhang, X., Zwiers, F. W., Li, G., Wan, H. & Cannon, A. J. Complexity in estimating past and future extreme short-duration rainfall. *Nat. Geosci.* **10**, 255–259 (2017).
32. Mahoney, K., Alexander, M. A., Thompson, G., Barsugli, J. J. & Scott, J. D. Changes in hail and flood risk in high-resolution simulations over Colorado Mountains. *Nat. Clim. Change* **2**, 125–131 (2012).
33. Brimelow, J. C., Burrows, W. R. & Hanesiak, J. M. The changing hail threat over North America in response to anthropogenic climate change. *Nat. Clim. Change* **7**, 516–522 (2017).
34. Craven, J. P., Brooks, H. E. & Hart, J. A. Baseline climatology of sounding derived parameters associated with deep, moist convection. *Natl Wea. Dig.* **28**, 13–24 (2004).
35. Prein, A. F. & Holland, G. J. Global estimates of damaging hail hazard. *Weather Clim. Extremes* **22**, 10–23 (2018).
36. McKee, T. B. & Doesken, N. J. *Colorado Extreme Storm Precipitation Data Study* Climatology Report No. 97–1 (Colorado State University, 1997).
37. Bradley, R. S., Keimig, F. T., Diaz, H. F. & Hardy, D. R. Recent changes in freezing level heights in the Tropics with implications for the deglacierization of high mountain regions. *Geophys. Res. Lett.* **36**, L17701 (2009).
38. Folkins, I. The melting level stability anomaly in the tropics. *Atmos. Chem. Phys.* **13**, 1167–1176 (2013).
39. Guerreiro, S. B. et al. Detection of continental-scale intensification of hourly rainfall extremes. *Nat. Clim. Change* **8**, 803–807 (2018).
40. Trenberth, K. E., Dai, A., Rasmussen, R. M. & Parsons, D. B. The changing character of precipitation. *Bull. Am. Meteorol. Soc.* **84**, 1205–1218 (2003).
41. Westra, S. et al. Future changes to the intensity and frequency of short-duration extreme rainfall. *Rev. Geophys.* **52**, 522–555 (2014).
42. Kendon, E. J. et al. Heavier summer downpours with climate change revealed by weather forecast resolution model. *Nat. Clim. Change* **4**, 570–576 (2014).
43. Ban, N., Schmidli, J. & Schär, C. Heavy precipitation in a changing climate: does short-term summer precipitation increase faster? *Geophys. Res. Lett.* **42**, 1165–1172 (2015).
44. Xie, B., Zhang, Q. & Wang, Y. Trends in hail in China during 1960–2005. *Geophys. Res. Lett.* **35**, L13801 (2008).
45. Allen, J. T. & Tippett, M. K. The characteristics of United States hail reports: 1955–2014. *E-J. Severe Storms Meteorol.* **10**, 3 (2015).

Methods

Observational datasets. We used four sources of observational data for our analysis: (1) RS data, (2) reanalysis data, (3) gauge-based and gridded precipitation records and (4) US and Australian hail observations.

Two sources of RS data were used. The first is the Integrated Global Radiosonde Archive Version 2[46], which is a quality-control dataset. However, jumps and other inconsistencies caused by changes in observing practice, instrumentation or station location have not been corrected. The second data source is the atmospheric sounding record from the Wyoming Weather Web[47]. Both datasets provide records at 00:00 and 12:00 universal coordinated time. We investigated the common period between 1979 and 2018 and only uses station records that were at least 80% complete in each year or season and had data for at least 80% of all years. This resulted in close to 500 stations globally.

We used two reanalyses, ERA-Interim[15] and ERA-20C[16]. ERA-Interim covers the period 1979 to present and has a horizontal grid spacing of approximately 80 km with 60 vertical levels. A large variate of in situ and remote sensing observations are assimilated (including RSs) from various data sources that can change over time. This can lead to discontinuities in the simulated time series[15]. ERA-Interim captures historical atmospheric states with a high accuracy compared to those of other reanalysis products[48,49].

ERA-20C has a horizontal grid spacing of approximately 125 km and 91 vertical levels[16]. It covers the period 1900–2010 and only assimilates surface pressure and surface marine wind observations. Changes in observational systems do introduce discontinuities, particularly in regions with sparse coverage, such as the Southern Hemisphere[50–53].

We used two datasets for rain and snow accumulations. The Global Historical Climatology Network station dataset provides quality-controlled rain and snowfall observations with global coverage[54]. The MSWEP V2 gridded precipitation dataset provides three-hourly precipitation estimates on a 0.1° grid globally from 1979 to 2017[55,56]. We used MSWEP V2 to calculate the daily precipitation rates at RS locations.

For analysis that include the maximum hail diameter, we used observations from the Storm Prediction Center's Storm Events dataset[57] and Australian Bureau of Meteorology's Severe Storms Archive[58] within the period 1979–2017.

Procedures. Wet-bulb temperature was calculated using air temperature and relative humidity[59]. The height of the zero wet-bulb temperature level above the surface was estimated by linearly interpolating between the two closest measurements that enclose the ML. This was done for each RS measurement and for six-hourly reanalysis output on model levels. If the surface wet-bulb temperature was below zero, the ML height was set to zero.

The mean CAPE and lifting condensation levels (cloud base hight) were calculated with the Python cape_2d algorithm. This algorithm first finds the maximum equivalent potential temperature (θ_e) height level in the lowest 3,000 m above ground. Centred on this level, a mean layer parcel with a depth of 500 m ascent was calculated.

Snow-day to precipitation-day ratios were calculated for events with more than 1 mm d^{-1} precipitation at all locations with a median of more than two snow days per year or season. For the reanalyses and the RSs, a snow probability parameterization was used, which is based on the near-surface wet-bulb temperature, surface temperature and low-level vertical-temperature lapse rate[60]. A snow day occurs if the snow probability is larger than 50% and the daily precipitation accumulation is larger than 1 mm (precipitation at the RS locations is derived from the nearest grid cell in the MSWEP dataset). We also used a 1 mm d^{-1} precipitation threshold for the analysis of WCL depth and associated precipitation changes. We also tested 2 and 5 mm d^{-1} thresholds to define wet days, which did not change the results substantially.

The relationship between daily average WCL depth/cloud base mixing ratio and the daily precipitation accumulation from MSWEP was calculated as follows for records with more than 1 mm d^{-1} precipitation. Daily precipitation accumulations were conditioned by binning daily mean WCL depth/cloud base mixing ratios by using bin intervals of 100 m/0.7 g kg^{-1} with a 250 m/1.5 g kg^{-1} overlap (for example, 2,000–2,500 m, 2,100–2,600 m and so on). Percentiles were calculated for bins with more than 1,000 precipitation records.

The SSP[34] was used to identify environments in which severe convective storms can develop. SSP is defined as the product of mean layer CAPE multiplied by mid-level vector shear (surface to a height of 6 km). SSP values larger than 10,000 $m^3 s^{-3}$ are statistically associated with hailstones larger than 2.5 cm in diameter.

Uncertainty estimates correspond to the spread between the RS, ERA-Interim and ERA-20C estimates.

The raw RS data were quality-controlled for non-physical outliers. The thresholds for outlier detection are summarized in Supplementary Table 1. RS observations were only considered if they had at least seven records below 300 hPa. Surface-to-ML lapse rates were only calculated if there were at least three records below the ML. CAPE and cloud base heights were only calculated for RSs with more than nine contiguous observations up to at least 150 hPa that monotonically increase in height above ground.

To remove non-homogeneous records, we tested all the annual average time series presented in this article (for example, ML height and WCL depth) for breaking points using the ruptures[61] package in Python. Four breakpoint detection algorithms were applied: (1) binary segmentation[62,63], (2) exact segmentation using the Pruned Exact Linear Time method[64], (3) bottom-up segmentation[65,66] and (4) window-based change point detection[67] with a width of 10 yr. In the first three methods, we used a penalty (P) to detect breakpoints with a magnitude of $P = \mathrm{std}(T)^{\log(N)}$ with T being the annual time series and N being the number of years in the time series. All the time series for which more than two of the four breaking-point detection algorithms identified a breaking point in the same year were removed from the analysis.

Data availability

The ERA-Interim and ERA-20C data used in this study are available from ECMWF's MARS archive (https://apps.ecmwf.int/datasets/). The Wyoming radiosonde dataset can be downloaded from http://weather.uwyo.edu/upperair/sounding.html. The Integrated Global Radiosonde Archive radiosonde data can be obtained from https://www.ncdc.noaa.gov/data-access/weather-balloon/integrated-global-radiosonde-archive. Global Historical Climatology Network data can be downloaded from https://www1.ncdc.noaa.gov/pub/data/ghcn/daily/by_year/. Maximum hail diameter reports are accessible from https://www.ncdc.noaa.gov/stormevents/ for the United States and from http://www.bom.gov.au/australia/stormarchive/ for Australia.

Code availability

The code for the statistical analysis and visualization of data in this document can be accessed under https://github.com/AndreasPrein/Increasing-Melting-Level-Height.git (ref. [68]).

References

46. Durre, I., Vose, R. S. & Wuertz, D. B. Overview of the integrated global radiosonde archive. *J. Clim.* **19**, 53–68 (2006).
47. Oolman, L. *Wyoming Weather Web* (University of Wyoming, accessed 10 June 2019); http://weather.uwyo.edu/upperair/sounding.html.
48. Lorenz, C. & Kunstmann, H. The hydrological cycle in three state-of-the-art reanalyses: intercomparison and performance analysis. *J. Hydrometeorol.* **13**, 1397–1420 (2012).
49. Fujiwara, M. et al. Introduction to the SPARC reanalysis intercomparison project (S-RIP) and overview of the reanalysis systems. *Atmos. Chem. Phys.* **17**, 1417–1452 (2017).
50. Berrisford, P. et al. Atmospheric conservation properties in ERA-Interim. *Q. J. R. Meteorol. Soc.* **137**, 1381–1399 (2011).
51. Simmons, A., Willet, K., Jones, P., Thorne, P. & Dee, D. Low-frequency variations in surface atmospheric humidity, temperature, and precipitation: inferences from reanalyses and monthly gridded observational data sets. *J. Geophys. Res. Atmos.* **115**, D01110 (2010).
52. Simmons, A. et al. Estimating low-frequency variability and trends in atmospheric temperature using ERA-Interim. *Q. J. R. Meteorol. Soc.* **140**, 329–353 (2014).
53. Trenberth, K. E., Zhang, Y., Fasullo, J. T. & Taguchi, S. Climate variability and relationships between top-of-atmosphere radiation and temperatures on Earth. *J. Geophys. Res. Atmos.* **120**, 3642–3659 (2015).
54. Menne, M. J., Durre, I., Vose, R. S., Gleason, B. E. & Houston, T. G. An overview of the global historical climatology network-daily database. *J. Atmos. Ocean. Technol.* **29**, 897–910 (2012).
55. Beck, H. E. et al. MSWEP: 3-hourly 0.25 global gridded precipitation (1979–2015) by merging gauge, satellite, and reanalysis data. *Hydrol. Earth Syst. Sci.* **21**, 589–615 (2017).
56. Beck, H. E. et al. MSWEP V2 global 3-hourly 0.1 precipitation: methodology and quantitative assessment. *Bull. Am. Meteorol. Soc.* **100**, 473–500 (2019).
57. Schaefer, J. & Edwards, R. The SPC tornado/severe thunderstorm database. In *Preprints, 11th Conf. on Applied Climatology, Dallas, TX* (American Meteorological Society, 1999).
58. *Severe Storms Archive* (Bureau of Meteorology, accessed 1 June 2018); http://www.bom.gov.au/australia/stormarchive/.
59. Knox, J. A., Nevius, D. S. & Knox, P. N. Two simple and accurate approximations for wet-bulb temperature in moist conditions, with forecasting applications. *Bull. Am. Meteorol. Soc.* **98**, 1897–1906 (2017).
60. Sims, E. M. & Liu, G. A parameterization of the probability of snow–rain transition. *J. Hydrometeorol.* **16**, 1466–1477 (2015).
61. Ruptures (ENS Paris-Saclay); http://ctruong.perso.math.cnrs.fr/ruptures-docs/build/html/index.html.
62. Bai, J. Estimating multiple breaks one at a time. *Econom. Theory* **13**, 315–352 (1997).
63. Fryzlewicz, P. et al. Wild binary segmentation for multiple change-point detection. *Ann. Stat.* **42**, 2243–2281 (2014).
64. Killick, R., Fearnhead, P. & Eckley, I. A. Optimal detection of changepoints with a linear computational cost. *J. Am. Stat. Assoc.* **107**, 1590–1598 (2012).
65. Fryzlewicz, P. Unbalanced Haar technique for nonparametric function estimation. *J. Am. Stat. Assoc.* **102**, 1318–1327 (2007).

66. Keogh, E., Chu, S., Hart, D. & Pazzani, M. An online algorithm for segmenting time series. In *Proc. 2001 IEEE International Conference on Data Mining* (eds Cercone, N., Lin, T. Y. & Wu, X.) 289–296 (IEEE, 2001).
67. Ahmed, E., Clark, A. & Mohay, G. A novel sliding window based change detection algorithm for asymmetric traffic. In *2008 IFIP International Conference on Network and Parallel Computing* (eds Cao, J., Li, M., Wu, M.-Y. & Chen, J.) 168–175 (IEEE, 2008).
68. Prein, A. F. *Increasing/Melting/Level/Height* (2020); https://doi.org/10.5281/zenodo.3677183.

Acknowledgements

NCAR is funded by the National Science Foundation. We thank the ECMWF, NOAA, NCDC and H. Beck for making available their datasets and K. E. Trenberth for his constructive comments. Computer resources were provided by the Computational and Information Systems Laboratory (NCAR Community Computing; http://n2t.net/ark:/85065/d7wd3xhc).

Author contributions

A.F.P. designed the study, and collected and analysed the data. A.J.H. provided conceptual advice and contributed to the writing.

Competing interests

The authors declare no competing interests.

Additional information

Extended data is available for this paper at https://doi.org/10.1038/s41558-020-0825-x.

Supplementary information is available for this paper at https://doi.org/10.1038/s41558-020-0825-x.

Correspondence and requests for materials should be addressed to A.F.P.

Peer review information *Nature Climate Change* thanks Kathleen Schiro and the other, anonymous, reviewer(s) for their contribution to the peer review of this work.

Reprints and permissions information is available at www.nature.com/reprints.

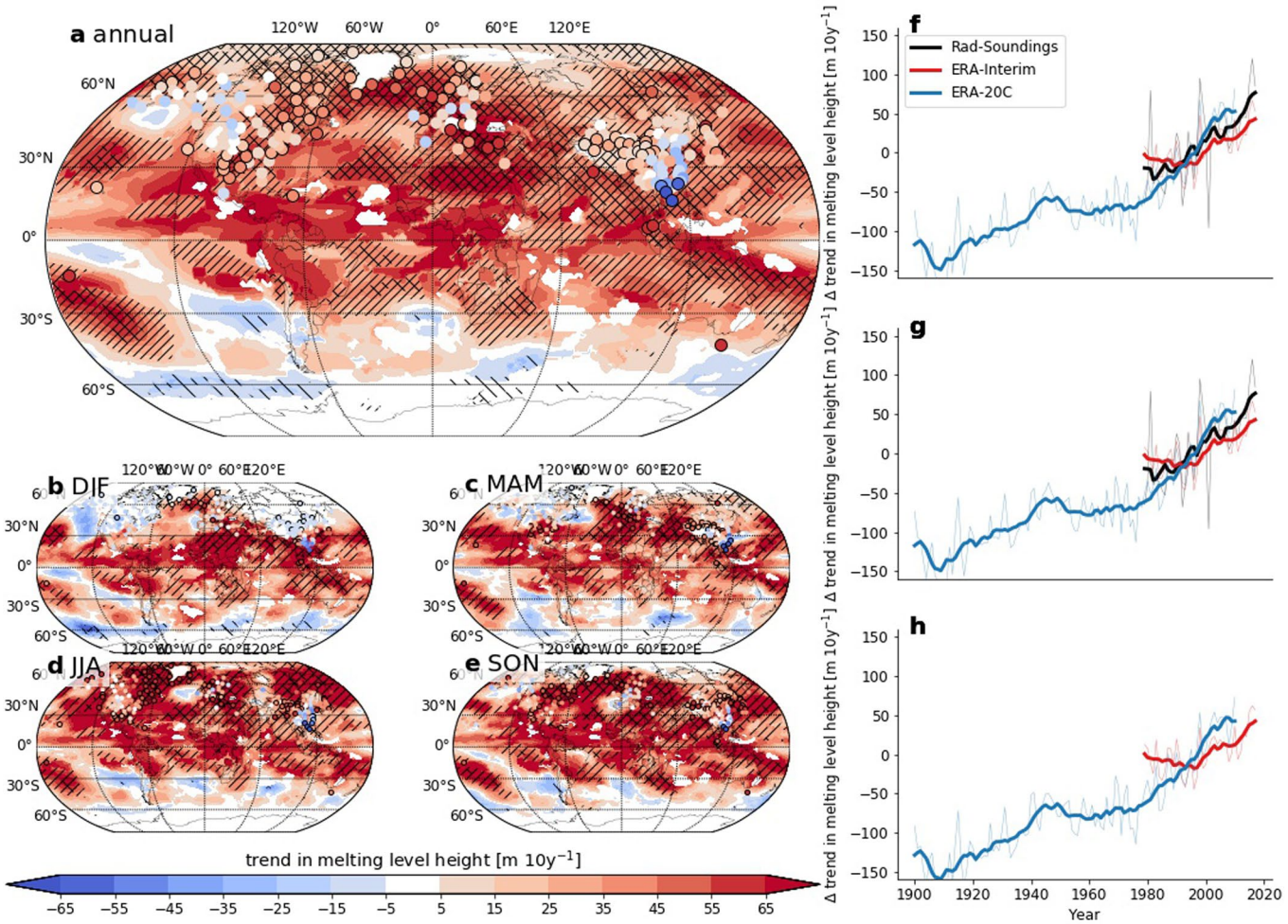

Extended Data Fig. 1 | Mean linear trend estimates of daily average melting level (ML) height from 1979 to 2010. Contours show annual average **a**, and seasonal (**b**–**e**) mean trends from ERA-Interim and ERA-20C and colored circles show trends from RS data. Hatching from top left to bottom right (bottom left to top right) shows areas where ERA-Interim (ERA-20C) has significant trends based on a two-sided Wald Test with t-distribution (α=0.05). Significant trends in RS data are shown with a back outlined circle. Average global, global land, and global ocean time series are shown in f–h. Thin lines show annual means and thick lines show ten-year moving averages.

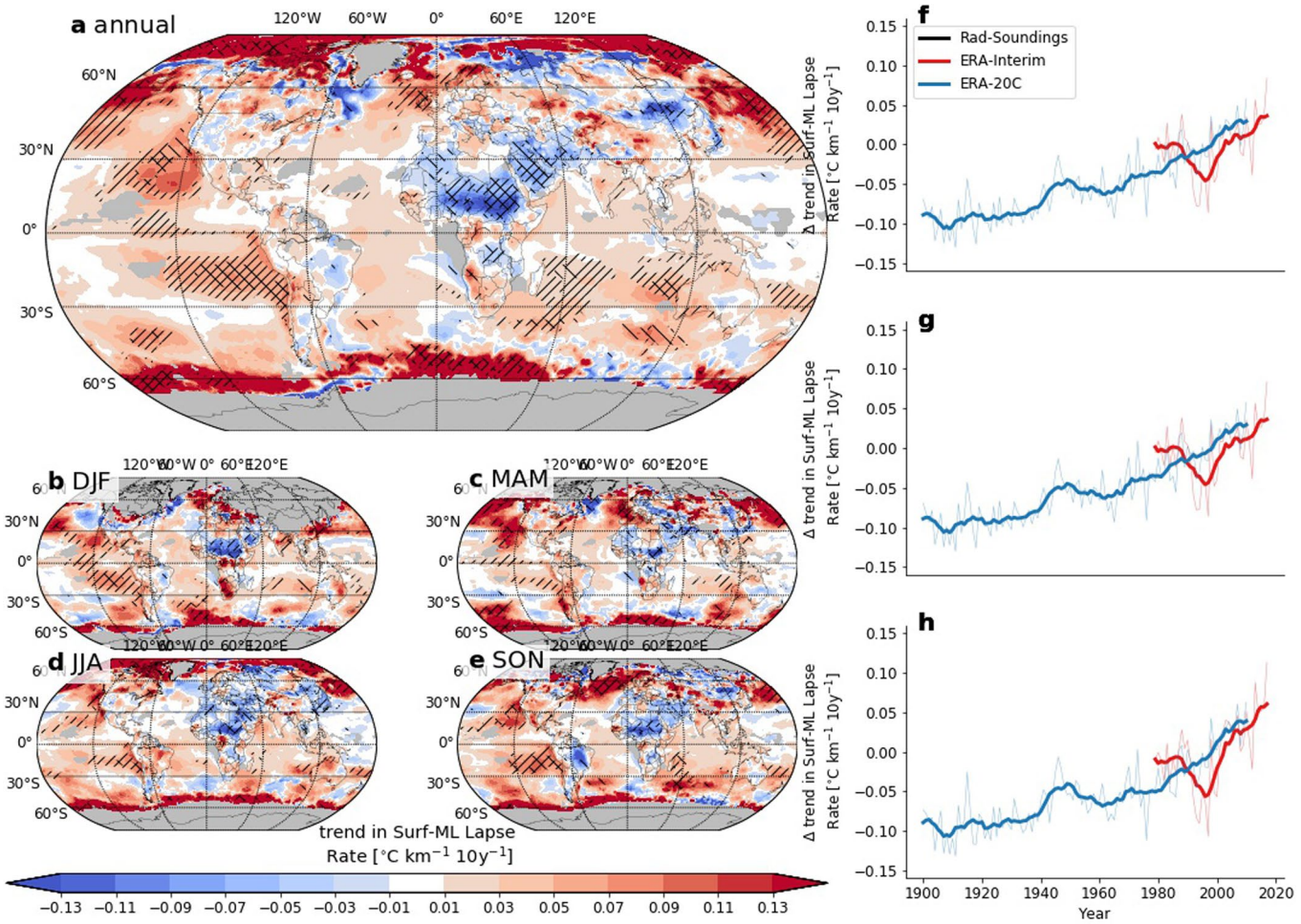

Extended Data Fig. 2 | Similar as Electronic Data Fig. 1 but for changes in the surface to melting level lapse rate (LR).

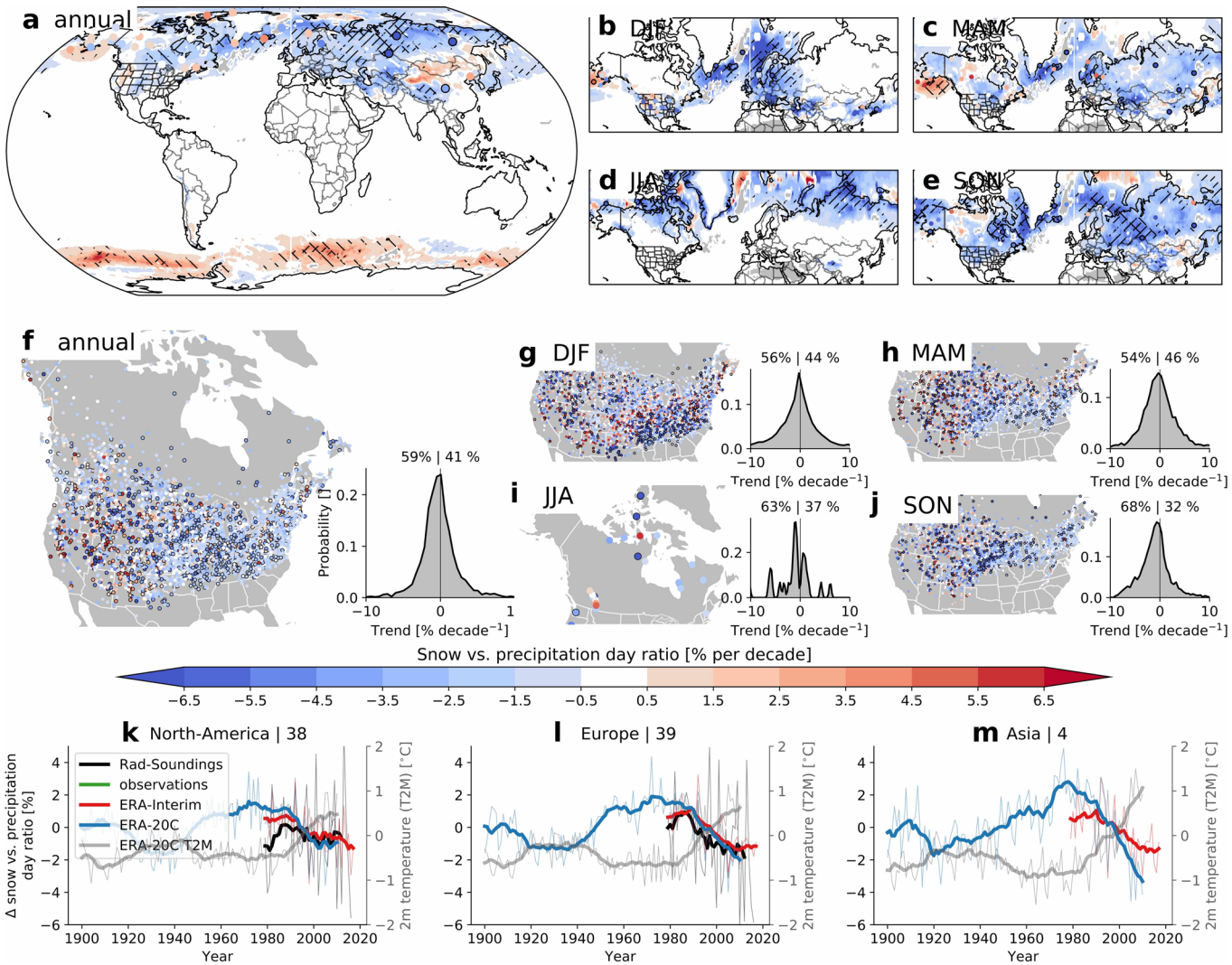

Extended Data Fig. 3 | Annual (a) and seasonal (b-e) linear trend estimates for snow-day to precipitation-day ratio (precipitation [liquid and solid] ≥ 1 mm d^{-1}) between 1979-2010. Filled contours show average trends from ERA-20C and ERA-Interim and filled circles show trends at radiosonde sounding stations. Right/left tilted hatched areas indicate that ERA-20c/ERA-Interim has statistically significant trends based on a two-sided Wald Test with t-distribution (α=0.05). Tick outlined circles show locations with significant radiosonde sounding trends. Panels (**f–j**) are similar to (**a–e**) but show observations from Global Historical Climatology Network (GHCN) stations. Tick outlined circles show locations with significant trends. The inlays show trend probability density functions including the ratio of negative and positive trends (numbers above inlay). Percent changes in the annual snow-day to precipitation-day ratio from ERA-20C (blue line), ERA-Interim (red line), radiosonde soundings (black line), and GHCN stations (green line; North America only) are shown for North America (**k**), Europe (**l**), and Asia (**m**) relative to the period 1979-2010. ERA-20C surface temperature (T2M) changes are shown in gray on the secondary y-axis. Thick lines show 10-year moving average values of annual data (thin lines).

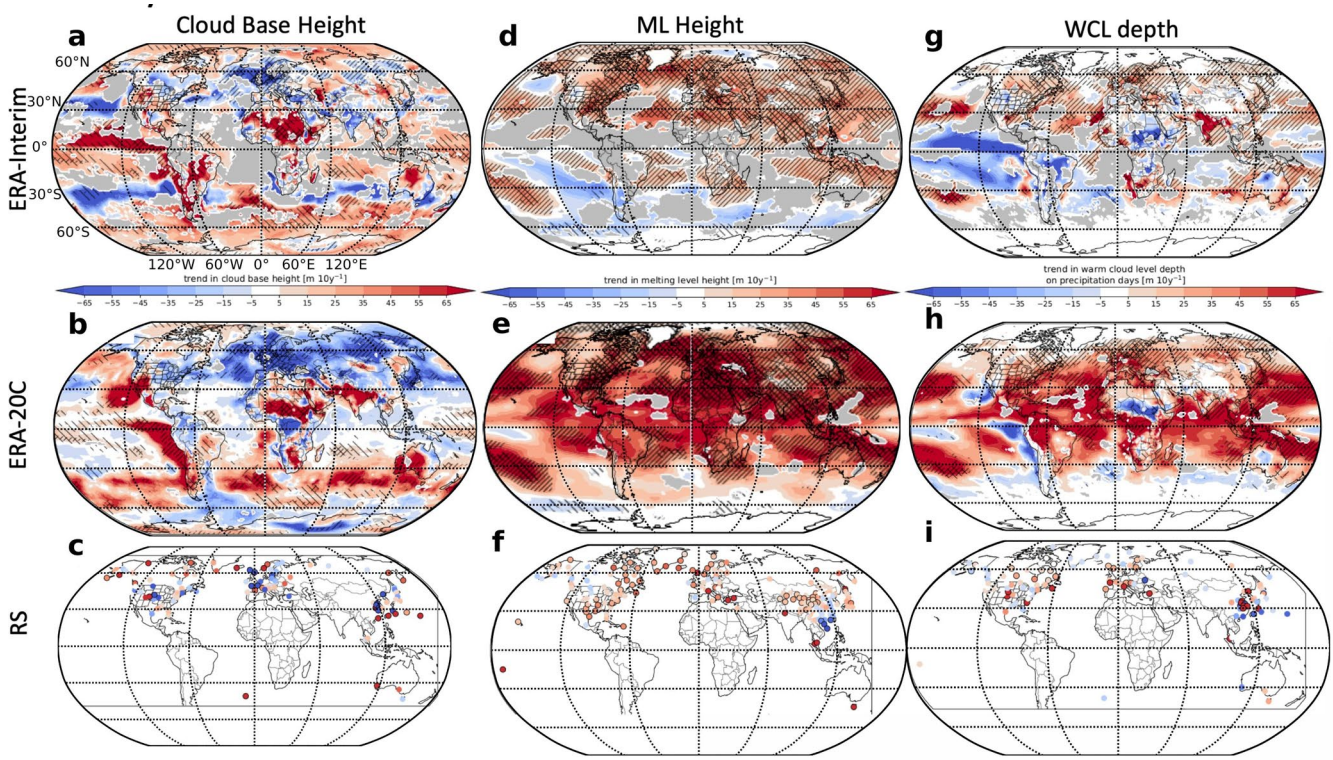

Extended Data Fig. 4 | Annual average linear trend estimates for cloud base height (a–c), melting level height (d–f), and warm cloud layer depth (g–i) from 1979 to 2010. Results are shown based on data from ERA-Interim (top row), ERA-20C (middle row), and radiosonde soundings (bottom row). Statistically significant trends are highlighted with hatching (ERA-Interim and ERA-20C) and with black outlined circles (radiosonde soundings) based on a two-sided Wald Test with t-distribution (α=0.05). Gray areas correspond to regions where breakpoints were detected.

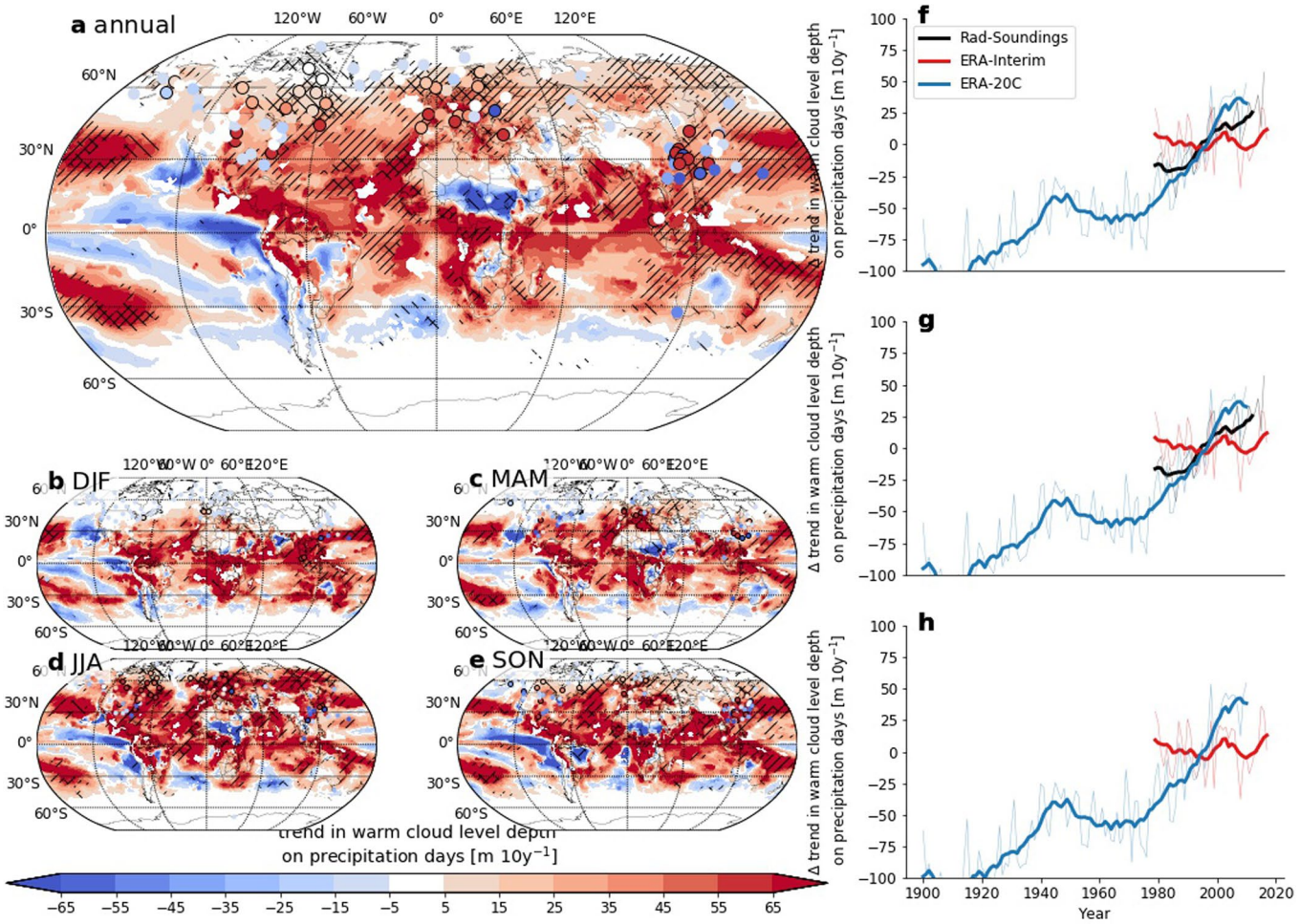

Extended Data Fig. 5 | Similar as Electronic Data Fig. 1 but for daily average warm cloud layer depth on precipitation days (days with > 1 mm d^{-1} precipitation).

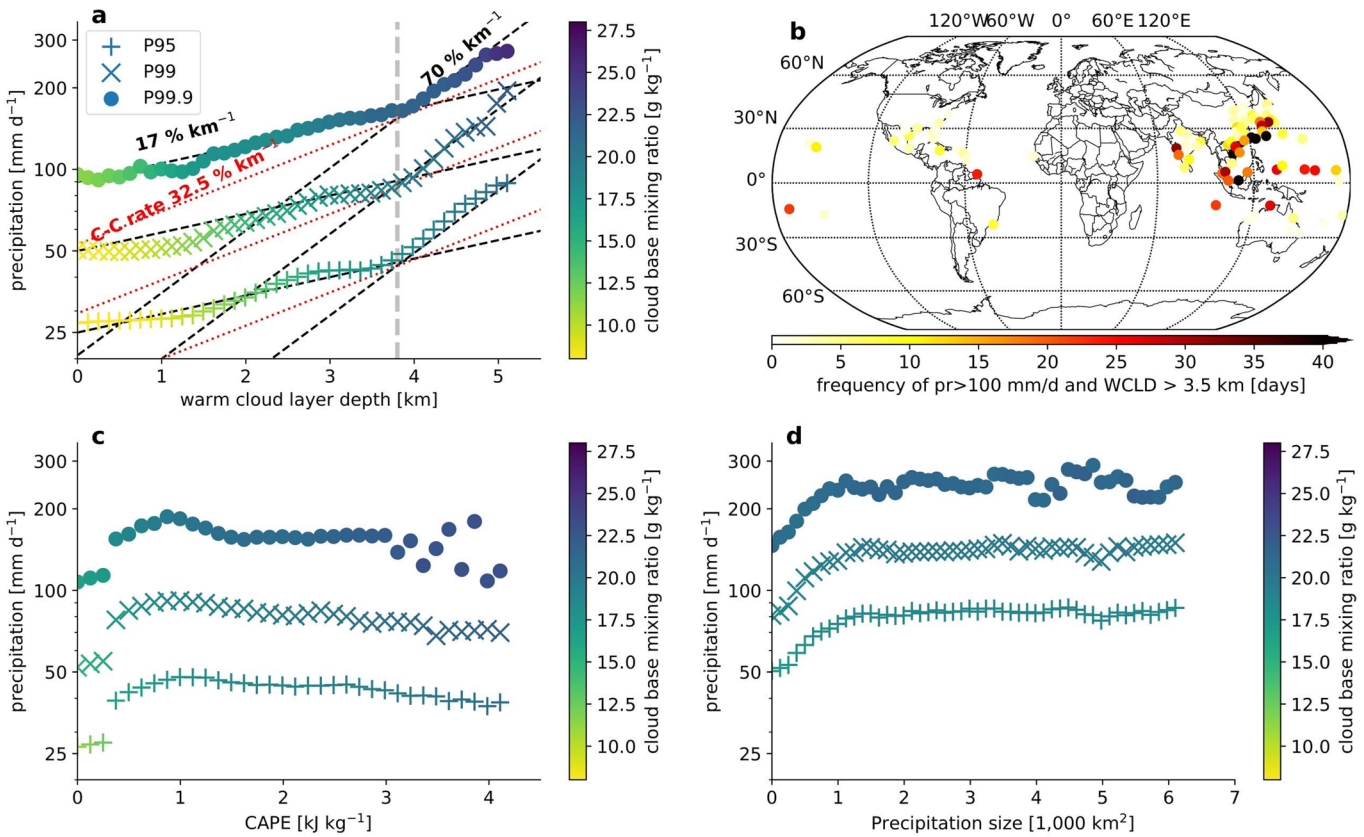

Extended Data Fig. 6 | Scaling of extreme precipitation with warm cloud layer (WCL) depth (a), convective available potential energy (CAPE, c), and the size of the rainfall producing precipitation object (d) on wet days (precipitation larger 1 mm). Results are based on daily averaged radiosonde soundings within the period 1979-2016. The symbol colors show the associated cloud base mixing ratio. Precipitation is conditioned by binning WCL depth/CAPE/precipitation size in bins of 124 m/kJ kg^{-1}/1,000 km^2 distance with 500 m/kJ kg^{-1}/1,000 km^2 overlap centred on each bin. (**b**) Frequency of daily precipitation accumulations larger than 100 mm under warm cloud layer depth (WCLD) conditions of greater 3.5 km.